waveguide layers calculated at four different wavelengths between 5 and 8 μm, which was our target wavelength range for supercontinuum emission. Figure 1b displays the resulting function $\alpha_w(\lambda)$.

Experience with quantum cascade laser design over a wide range of wavelengths[7,8,19] also allowed us to put the additional constraint that

$$g_i^*(\lambda) = \frac{4\pi}{\epsilon_0 hcn_{\text{eff}}}\tau_{3,i}\left(1 - \frac{\tau_{2,i}}{\tau_{32,i}}\right)z_i^2\frac{1}{L_i}\cdot\frac{1}{\lambda_{0,i}} \approx \text{constant} \quad (3)$$

which is equivalent to predetermining the peak gain coefficient for every active region stage i. The insets in Fig. 1c show the schematic conduction band diagrams of two active regions (at 5 and 8 μm wavelength, respectively), which satisfy condition (3). Finally, prior experimental work[7,8,19] allows us to use the approximation that $\Delta\lambda_i = 0.1\cdot\lambda_{0,i}$.

Having introduced this set of constraints—which is only one of a very large number of possible sets—a family of solutions to equation (1b) can now be found, which acts as a design rule for supercontinuum light generation. This design rule simply gives the peak wavelength $\lambda_{0,i}$ as a function of i. However, the family of solutions is still rather large, owing to permutations of active regions across the symmetry plane at the very centre of the waveguide. We can narrow it down in the following way: the injector regions (see below) are easier to design if adjacent active regions do not differ much in emission wavelength. Therefore we add the constraint that $\lambda_{0,i}$ be a monotonic function of i. Figure 1c then shows the final result, $\lambda_{0,i}$ versus i.

IS transition active regions

The 'three-well vertical transition'[19] active region consists of three InGaAs quantum wells closely coupled by thin AlInAs barriers. Figure 1c shows two examples at a design electric field of 60 kV cm^{-1}. Laser action occurs between the upper (3) and lower (2) laser levels, respectively. The computed LO phonon scattering time $\tau_{32,i}$ between the two levels ranges from 3.1 to 2.2 ps for wavelengths from 5 to 8 μm, respectively. Level 2 is closely coupled to ground state 1 of the active region. Their energy separation is chosen as ≤ 40 meV, designed to efficiently deplete the lower laser level 2 of electrons via resonant LO phonon scattering; the energy of the LO phonon in the InGaAs/AlInAs material system is approximately 34 meV. The corresponding scattering lifetime is calculated as $\tau_{2,i} \approx 0.3$ ps, which is much smaller than $\tau_{32,i}$, so that population inversion between levels 3 and 2 is readily achieved and laser action is possible.

Injector regions

Consecutive active regions are bridged by so-called injector regions. These are regions of five to six quantum wells closely coupled with narrow barriers, such that a 'miniband'—a dense manifold of energy levels—is formed, which allows efficient carrier transport. Electrons tunnelling out of levels 2 and 1 of the preceding active region traverse the injector region through this miniband and are re-injected by tunnelling into level 3 of the following downstream active region. This is the essence of the cascading process of quantum cascade lasers[7,8,19]. The centre portion of each injector region is furthermore doped to an electron sheet density of $\sim 1.6\times10^{11}$ cm^{-2} per injector, thus providing stable current flow by preventing space charge build-up.

Received 25 October; accepted 28 December 2001.

1. Mittelstein, M. *et al.* Broadband tunability of gain-flattened quantum well semiconductor lasers with an external grating. *Appl. Phys. Lett.* **54,** 1092–1094 (1989).
2. Hall, D. C. *et al.* Broadband long-wavelength operation (9700 Å ≥ λ ≥ 8700 Å) of $Al_yGa_{1-y}As$-GaAs-$In_xGa_{1-x}As$ quantum well heterostructure lasers in an external grating cavity. *Appl. Phys. Lett.* **55,** 752–754 (1989).
3. Chernikov, S. V. *et al.* Supercontinuum self-Q-switched ytterbium fiber laser. *Opt. Lett.* **22,** 298–300 (1997).
4. Fuke, A., Masuda, K. & Tokita, Y. High power He-Cd$^+$ white light laser. *AIP Conf. Proc.* **160,** 229–231 (1987).
5. Spielmann, C. *et al.* Ultrabroadband femtosecond lasers. *IEEE J. Quantum Electron.* **30,** 1100–1114 (1994).
6. Ranka, J. K., Windeler, R. S. & Stentz, A. J. Visible continuum generation in air silica microstructure optical fibers with anomalous dispersion at 800nm. *Opt. Lett.* **25,** 25–27 (2000).
7. Capasso, F. *et al.* New frontiers in quantum cascade lasers and applications. *IEEE J. Select. Topics Quantum Electron.* **6,** 931–947 (2000).
8. Gmachl, C., Capasso, F., Sivco, D. L. & Cho, A. Y. Recent progress in quantum cascade lasers and applications. *Rep. Prog. Phys.* **64,** 1533–1601 (2001).
9. Collings, B. C., Mitchell, M. L., Boivin, L. & Knox, W. H. A 1021 channel WDM system. *Opt. Photon. News* **11,** 31–35 (2000).
10. Jones, D. J. *et al.* Carrier-envelope phase control of femtosecond mode-locked lasers and direct optical frequency synthesis. *Science* **288,** 635–639 (2000).
11. Schiff, H. I., Mackay, G. I. & Bechara, J. in *Air Monitoring by Spectroscopic Techniques* (ed. Sigrist, M. W.) Ch. 5, 239–333 (Wiley Interscience, New York, 1994).
12. Campman, K. L., Schmidt, H., Imamoglu, A. & Gossard, A. C. Interface roughness and alloy-disorder scattering contributions to intersubband transition linewidths. *Appl. Phys. Lett.* **69,** 2554–2556 (1996).
13. Capasso, F. Band-gap engineering: from physics and materials to new semiconductor devices. *Science* **235,** 172–176 (1987).
14. Muravjov, A. V., Withers, S. H., Pavlov, S. G., Shastin, V. N. & Peale, R. N. Broad band p-Ge optical amplifier of terahertz radiation. *J. Appl. Phys.* **86,** 3512–3515 (1999).
15. Faist, J. *et al.* Quantum cascade laser. *Science* **264,** 553–556 (1994).
16. Cho, A. Y. (ed.) *Molecular Beam Epitaxy* (AIP Press, Woodbury, New York, 1994).
17. Sirtori, C. *et al.* Quantum cascade laser with plasmon-enhanced waveguide operating at 8.4 μm wavelength. *Appl. Phys. Lett.* **66,** 3242–3244 (1995).
18. Gmachl, C. *et al.* Quantum cascade lasers with a heterogeneous cascade: Two-wavelength operation. *Appl. Phys. Lett.* **79,** 572–574 (2001).
19. Faist, J. *et al.* High-power mid-infrared (λ ~ 5 μm) quantum cascade lasers operating above room temperature. *Appl. Phys. Lett.* **68,** 3680–3682 (1996).

Acknowledgements

We thank S. N. G. Chu for help with material characterization, in particular transmission electron microscopy; T. S. Mosely and A. Straub for help with measurements; and D. A. Ackerman for discussions. This work was supported in part by DARPA/US Army Research Office.

Competing interests statement

The authors declare that they have no competing financial interests.

Correspondence should be addressed to C.G. (e-mail: cg@lucent.com).

Three-dimensional X-ray structural microscopy with submicrometre resolution

B. C. Larson*, Wenge Yang*, G. E. Ice†, J. D. Budai* & J. Z. Tischler*

** Solid State Division, † Metals & Ceramics Division, Oak Ridge National Laboratory, PO Box 2008, Oak Ridge, Tennessee 37831, USA*

Advanced materials and processing techniques are based largely on the generation and control of non-homogeneous microstructures, such as precipitates and grain boundaries. X-ray tomography can provide three-dimensional density and chemical distributions of such structures with submicrometre resolution[1]; structural methods exist that give submicrometre resolution in two dimensions[2–8]; and techniques are available for obtaining grain-centroid positions and grain-average strains in three dimensions[7,9]. But non-destructive point-to-point three-dimensional structural probes have not hitherto been available for investigations at the critical mesoscopic length scales (tenths to hundreds of micrometres). As a result, investigations of three-dimensional mesoscale phenomena—such as grain growth[10,11], deformation[12–16], crumpling[17–19] and strain-gradient effects[20]—rely increasingly on computation and modelling without direct experimental input. Here we describe a three-dimensional X-ray microscopy technique that uses polychromatic synchrotron X-ray microbeams to probe local crystal structure, orientation and strain tensors with submicrometre spatial resolution. We demonstrate the utility of this approach with micrometre-resolution three-dimensional measurements of grain orientations and sizes in polycrystalline aluminium, and with micrometre depth-resolved measurements of elastic strain tensors in cylindrically bent silicon. This technique is applicable to single-crystal, polycrystalline, composite and functionally graded materials.

We have developed a differential-aperture X-ray microscopy (DAXM) technique to make microstructure and stress/strain measurements with submicrometre point-to-point spatial resolution in three dimensions. DAXM exploits knife-edge step profiling to provide a micrometre-resolution X-ray slit with high angular acceptance, in connection with charge-coupled device (CCD) X-ray area detection and computer reconstruction of Laue diffraction patterns from polychromatic X-ray microbeams. Using this method, complete Laue diffraction patterns are extracted as a function of depth along the penetration direction of the microbeam.

© 2002 Macmillan Magazines Ltd

The technique is analogous to a translating pinhole camera, and provides access to full diffraction information from submicrometre voxels (volume elements) in bulk materials. Submicrometre transverse resolution is provided by the use of ~0.5-μm-diameter microbeams, and data collection and diffraction pattern analyses are handled by previously developed[7] computer indexing and crystallographic analyses[21,22].

Figure 1 shows the geometry for polychromatic microbeam Laue diffraction measurements. It also illustrates the method for obtaining depth-resolved Laue patterns from bulk samples. After collecting a CCD image with the wire at position (n), the wire is stepped to position ($n+1$) where a second CCD image is collected. The source of the differential intensity $[I(n)-I(n+1)]$ in each pixel of the detector can be uniquely assigned to length segments along the microbeam using the position of the profiling wire and the position of individual CCD pixels. This is illustrated by the intensity of the (hkl) reflection emanating from a voxel in the centre of the grain shown in Fig. 1. Continuing the process of stepping the wire across the diffraction pattern, the corresponding differential intensities for the ($h'k'l'$) and ($h''k''l''$) reflections are generated in a similar manner. Computer collation of the pixel-by-pixel differential intensities provides a submicrometre-resolution spatial mapping of the entire Laue diffraction pattern onto the source of the scattering along the incident microbeam. The pixel positions, the geometrical parallax associated with the ($\sim 20\times 20\ \mu m^2$) pixel size, and the step size, step direction, and the circular shape of the Pt wire are taken into account. The wire may be stepped at an angle to the microbeam if desired (Fig. 2). It is necessary for the overall precision and accuracy of the method that $D_{XR} \ll D_{CCD}$ (see Fig. 1). This condition ensures that the parallax correction due to CCD pixel size is small, and that the spatial resolution of the reconstructed diffraction patterns is determined primarily by the step size of the Pt wire differential aperture. Therefore, depth resolution significantly smaller than a micrometre is readily achievable.

The individual reconstructed Laue diffraction patterns are analysed using previously developed[7,21,22] computer indexing, crystallographic orientation, and stress/strain tensor analyses. Computer-automated peak searches locate the positions of Bragg reflections, and pattern recognition software crystallographically indexes the diffraction pattern. Formally, measured diffraction patterns correspond to Bragg scattering spots from a crystal with an orientation matrix, A_M, that is in turn related to the orientation matrix, A_o, for an undistorted crystal that is aligned with the laboratory reference frame by:

$$A_M = TRA_o \qquad (1)$$

Here R and T specify, respectively, the (rigid) angular rotation matrix and the elastic distortion matrix of the diffracting grain relative to undistorted material aligned with the laboratory reference system. The components of R and T contain the local structural information that is desired. They are determined by nonlinear least-squares fitting of the crystal orientation and strain components such that Bragg peak positions calculated using A_M fit the measured Laue diffraction pattern. White beam diffraction patterns are sensitive to the structure and orientation of unit cells in a crystal, and to the relative magnitude of the lattice spacings[7,21]. Therefore, the orientation and the deviatoric (that is, shear) strain components result directly from the Laue diffraction patterns. Absolute lattice parameters and dilatational strains require an independent specification of one lattice spacing, such as by insertion of a monochromator to measure the energy of at least one Bragg reflection in the Laue pattern[7,21,22].

Figure 2 illustrates the use of the DAXM technique to make micrometre-resolution measurements of grain sizes and both intra- and intergranular orientations in a bulk polycrystalline material. Figure 2a shows the geometry for a microbeam probing a hot-rolled (200 °C) polycrystalline aluminium alloy (Al with 1% Fe,Si); Fig. 2b shows the superpositioned Laue diffraction patterns of the many grains illuminated by the microbeam. Microbeam generation on the Sector 7 undulator beamline at the Advanced Photon Source (at Argonne National Laboratory) has been described previously[7,22]. Depth profiling and computer reconstruction of Laue diffraction patterns as a function of depth by the DAXM profiling technique produces a series of individual depth-resolved Laue diffraction patterns such as the one shown in Fig. 2c. Automatic computer indexing and crystallographic orientation/distortion analyses of the individual diffraction patterns following equation (1) was used to extract individual orientation matrices and strain tensors as a function of depth along the microbeam. These micrometre-by-micrometre orientations provide a direct measure of individual grain sizes (along the microbeam) and intra- as well as intergranular rotations. This is shown for the first 80 μm in Fig. 2d. In this case, the microbeam entered the sample at a 45° angle to the surface in the plane defined by the sample normal direction (ND) and the rolling direction (RD).

Grain and subgrain boundaries (identified by positions with non-zero rotations in Fig. 2d) indicate crystal sizes ranging from a few micrometres to ~10 μm. These sizes are consistent with the microbeam passing near grain-boundary triple junctions and the grain sizes observed in the bright-field transmission electron microscopy image in Fig. 2a, which was made on a similar hot-rolled polycrystalline Al sample (H. Weiland provided the sample and the image). Because full orientation matrices are determined for each micrometre, detailed depth-dependent ⟨hkl⟩ orientation maps (that is, (hkl) pole figures or orientation distribution functions) can be constructed. For instance, the (111) pole figures in Fig. 2d show a variation in orientation correlations for regions of <10° rotation angles (subgrains) as compared with regions of larger (>10°) intergranular rotation angles (grains). However, the power of these measurements will be in direct studies of local polycrystalline structure, rather than the generation of statistical orientation correlations[23,24].

The elastic strain tensors measured in polycrystalline Al will not be discussed here as they are relatively small and have not been analysed in detail. Rather, we illustrate micrometre-resolution strain tensor measurements using the large elastic strains (and strain gradients) in cylindrically bent Si. Cylindrically bent plates, spherical shells, developed cones, and crumpling in thin sheets[17–19] have been of long-standing[25,26] fundamental and technological

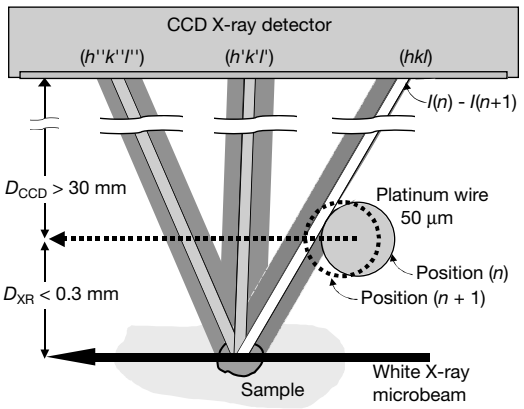

Figure 1 Differential-aperture X-ray (structural) microscopy depth-profiling method. Schematic view of a white microbeam penetrating a sample and scattering into a CCD area detector. Bragg scattering for the (hkl), ($h'k'l'$) and ($h''k''l''$) Laue reflections is depicted for a single grain and for a small segment (or voxel) in the interior of the grain. A Pt wire profiler is shown at position (n) and the dashed circle indicates the ($n+1$) position of the wire after a submicrometre step.

© 2002 Macmillan Magazines Ltd

interest dating to Euler's elastica[25] for beam deflection. The coupling of stretching and bending produces the stiffness and strength associated with structures ranging from aeroplane wings to microelectromechanical systems. Although the overall principles have been clear, only recently have topographical details associated with elastic instabilities and crumpling in thin bent plates been addressed in detail[17–19], and the local stress/strain distributions have yet to be investigated experimentally.

Figure 3 depicts the geometry for depth-dependent measurements of elastic strain tensors in a 25-μm-thick ⟨001⟩ oriented Si plate with ⟨110⟩ edges that was bent to a radius $R = 3.3$ mm at the apex of the arch. The gradient of the strain component ϵ_{xx} in the z direction for cylindrical bending around the y axis is given geometrically by $\nabla\epsilon_{xx} = 1/R$. Silicon responds elastically[27] at room temperature; moreover, except for positions very near the edge of the plate, the anticlastic strain ϵ_{yy} is vanishingly small for thin, cylindrically bent plates[26]. Separating strain into deviatoric (shear) components, ϵ'_{ij}, and isotropic dilatation components, $\mathrm{Tr}\epsilon_{ij}/3$, ϵ_{ij} is defined by

$$\epsilon_{ij} \equiv \epsilon'_{ij} + [\mathrm{Tr}\epsilon_j/3]\, I_{ij} \qquad (2)$$

where I_{ij} is the identity matrix, $\mathrm{Tr}\epsilon_{ij}$ is the trace of ϵ_{ij}, and ϵ'_{ij} is to be obtained directly from the analysis of white beam Laue patterns. In the present case, we note that $\mathrm{Tr}\epsilon_{ij}/3 = -\epsilon'_{yy}$ (since $\epsilon_{yy} \approx 0$). Figure 3b shows the depth-integrated Laue diffraction pattern (streaked) from the bent Si sample, and the superposition of depth-resolved Laue diffraction patterns (non-streaked) for 1-μm-thick slices near the top and bottom surfaces of the silicon arch, as resolved by the DAXM analysis.

Figure 4a shows deviatoric strain tensor measurements for cylindrically bent Si and for a flat (that is, strain-free) Si sample. The results for unstrained Si fluctuate near zero within the ($\pm 1 \times 10^{-4}$) uncertainties of our present strain tensor measurement capabilities. As expected, the deviatoric strain measurements for bent Si show large elastic tensile and compressive strains along the x direction at the top and bottom surfaces, respectively. As indicated above, the non-zero ϵ'_{yy} (deviatoric strain) provides a direct measure of $-\mathrm{Tr}\epsilon_{ij}/3$, which represents the isotropic dilatational strain as a function of depth in the Si plate. By fitting a straight line to ϵ'_{yy} as a function of depth and adding $\mathrm{Tr}\epsilon_{ij}/3$ to each of the diagonal components of ϵ'_{ij}, we obtain the full elastic strain ϵ_{ij} plotted in Fig. 4b.

The depth dependence (gradient) of ϵ_{xx} in Fig. 4b is in good agreement with the solid line, which has a slope corresponding to $\sin(45°)/(3.3\ \mathrm{mm})$. This is the inverse of the radius of curvature measured at the apex of the arch, allowing for the 45° incident angle

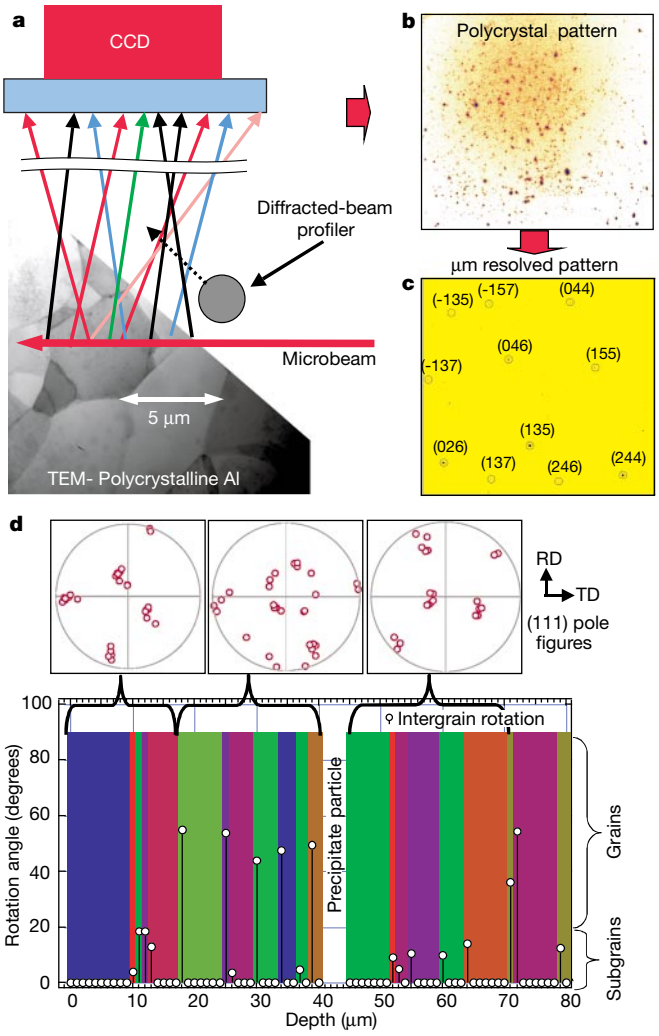

Figure 2 DAXM probe of the grain structure in polycrystalline Al. **a,** Schematic view of Bragg diffraction by a polychromatic X-ray microbeam superposed on a transmission electron microscopy image of hot-rolled polycrystalline Al; the microbeam diffraction pattern is collected by a CCD area detector as a Pt wire profiler is stepped along the sample surface. **b**, CCD image of the superpositioned Laue diffraction patterns from the polycrystalline Al sample in **a**. **c**, Example of a micrometre-resolution depth-resolved Laue diffraction pattern and the crystallographic indexation. **d**, Micrometre-resolution intra- and intergranular rotation angles for 1-μm steps along the microbeam; the open circles denote the local crystal rotation angle (or disorientation) relative to the previous position. The boxes above the rotation angle plot are depth-dependent (111) pole figures for the depths defined by the braces; TD is the transverse direction. The Laue patterns for depths of 40–44 μm could not be indexed as f.c.c. structures, and are probably from a precipitate particle in the Al(1%Si,Fe) alloy.

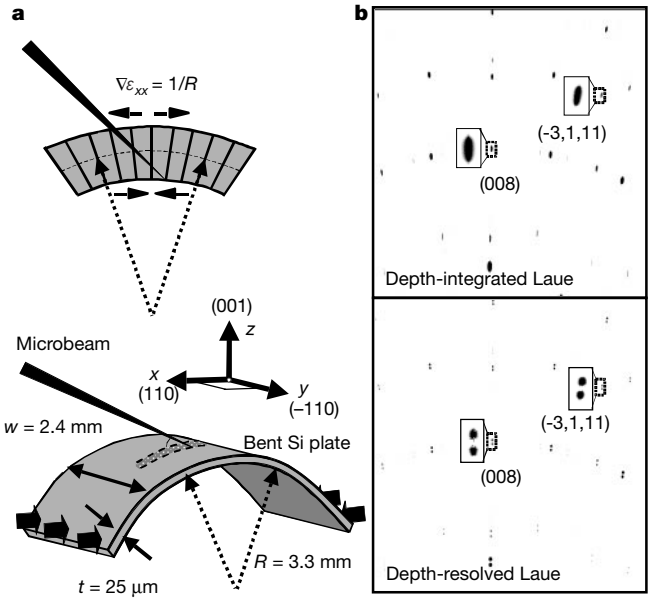

Figure 3 DAXM orientation and strain measurements in cylindrically bent Si. **a**, Illustration of the strain gradient in a thin, bent plate and the X-ray microbeam geometry used for strain tensor measurements. **b**, Polychromatic microbeam diffraction pattern from cylindrically bent Si (top panel), and depth-resolved diffraction patterns extracted by DAXM for 1-μm layers near the top and bottom surfaces of the plate (bottom panel). The enlarged views for the (008) and (–3,1,11) reflections indicate the effects of bend-induced strain and the (0.0123° per μm) bend-induced rotations along the beam direction.

© 2002 Macmillan Magazines Ltd

of the beam. Similar agreement exists between the gradient of ϵ_{zz} and that expected using the anisotropic Poisson's ratio for this deformation geometry. As the bent Si lattice contains rotations introduced by the cylindrical bend as well as steep elastic strain gradients along the direction of the X-ray microbeam, these measurements demonstrate that it is possible to determine both the local lattice orientation and the local strain tensor in materials where both are changing continuously.

The availability of point-to-point three-dimensional submicrometre-resolution X-ray diffraction measurements using DAXM provides a direct—and previously missing—link between the actual microstructure and evolution in materials and the results of numerical simulations and multi-scale modelling of microstructure and evolution on mesoscopic length scales. The results reported here indicate that the DAXM method could be used for many classes of structure, microstructure and local stress/strain investigations. Examples include fundamental intra- and intergranular studies of polycrystalline evolution[11,23,24] in three dimensions, fracture and the brittle-to-ductile transformation[27,28], crumpling in plates and shells[17–19,26], and fundamental plastic deformation investigations[15,20,29,30] including materials length scales, strain-gradient effects, and direct linkage with theory and simulations. Penetration depths will be restricted in high-Z materials and background levels will be limitations in some cases, as will reductions in spatial resolution for low scattering angles. However, modifications and extensions of the technique can be anticipated that would enhance its capabilities—as well as potentially extending the range of applications to geological, environmental, biological, structural mechanics and other disciplines, in addition to the materials physics applications addressed here. □

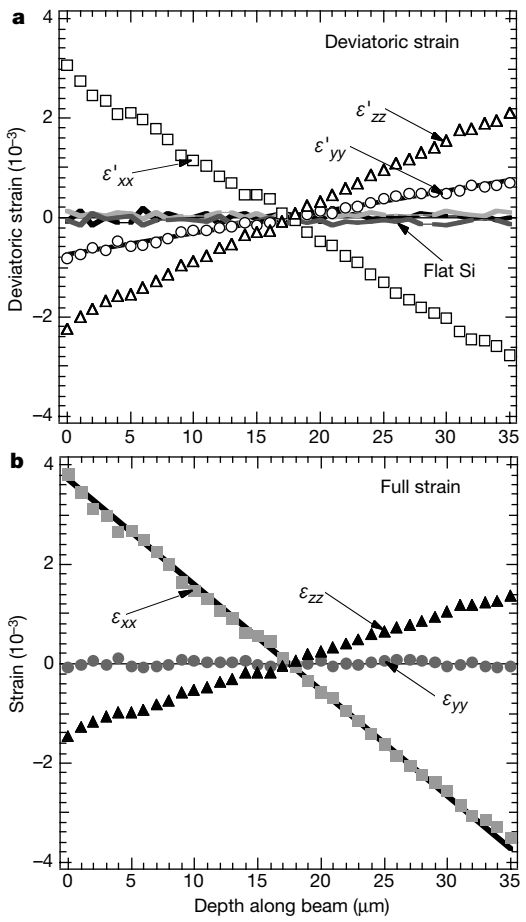

Figure 4 Depth-dependent strain tensor measurements for cylindrically bent Si. **a**, Diagonal components of the deviatoric strain tensors measured in a 25-μm-thick flat Si plate and a 25-μm-thick cylindrically bent (3.3-mm radius) Si plate. **b**, Diagonal components of the full strain tensor (deviatoric + dilatational) in cylindrically bent Si; the solid line indicates the slope of ϵ_{xx} expected for $R = 3.3$ mm.

Received 6 September 2001; accepted 3 January 2002.

1. Wang, Y. *et al.* A high-throughput x-ray microtomography system at the advanced photon source. *Rev. Sci. Instrum.* **72,** 2062–2068 (2000).
2. Di Fonzo, S. *et al.* Non-destructive determination of local strain with 100-nanometre spatial resolution. *Nature* **403,** 638–640 (2000).
3. Bilderback, D. H., Hoffman, S. A. & Thiel, D. J. Nanometer spatial-resolution achieved in hard x-ray-imaging and Laue diffraction experiments. *Science* **263,** 201–203 (1994).
4. Yun, W. *et al.* Nanometer focusing of hard x rays by phase zone plates. *Rev. Sci. Instrum.* **70,** 2238–2241 (1999).
5. Lengeler, B. *et al.* A microscope for hard x rays based on parabolic compound refractive lenses. *Appl. Phys. Lett.* **74,** 3924–3926 (1999).
6. Field, D. Recent advances in the application of orientation imaging. *Ultramicroscopy* **67,** 1–9 (1997).
7. Ice, G. E. & Larson, B. C. 3D x-ray crystal microscope. *Adv. Eng. Mater.* **2,** 643–646 (2000).
8. MacDowell, A. A. *et al.* Submicron x-ray diffraction. *Nucl. Instrum. Methods A* **467,** 936–943 (2001).
9. Margulies, L., Winther, G. & Poulsen, H. F. In situ measurement of grain rotation during deformation of polycrystals. *Science* **292,** 2392–2394 (2001).
10. Holm, E. A., Zacharopoulos, N. & Srolovitz, D. J. Nonuniform and directional grain growth caused by grain boundary mobility variations. *Acta. Mater.* **46,** 953–964 (1998).
11. Radhakrishnan, B., Sarma, G. B. & Zacharia, T. Modeling the kinetics and microstructural evolution during static recrystallization—Monte Carlo simulation of recrystallization. *Acta Mater.* **46,** 4415–4433 (1998).
12. Bulatov, V., Abraham, F. F., Kubin, L., Devincre, B. & Yip, S. Connecting atomistic and mesoscale simulations of crystal plasticity. *Nature* **391,** 669–672 (1998).
13. Cleri, F., Yip, S., Wolf, D. & Phillpot, S. R. Atomic-scale mechanism of crack-tip plasticity: dislocation nucleation and crack-tip shielding. *Phys. Rev. Lett.* **79,** 1309–1312 (1997).
14. De la Rubia, T. D. *et al.* Multiscale modelling of plastic flow localization in irradiated materials. *Nature* **406,** 871–874 (2000).
15. Gao, H., Huang, Y. & Nix, W. D. Modeling plasticity at the micrometer scale. *Naturwissenschaften* **86,** 507–515 (1999).
16. Vashishta, P., Kalia, R. K. & Nakano, A. Large-scale atomistic simulations of dynamic fracture. *Comput. Sci. Eng.* **1,** 56–65 (1999).
17. Boudaod, A., Patrício, P., Couder, Y. & Amar, M. B. Dynamics of singularities in a constrained elastic plate. *Nature* **407,** 718–720 (2000).
18. Chaïeb, S., Melo, F. & Géminard, J.-C. Experimental study of developable cones. *Phys. Rev. Lett.* **80,** 2354–2357 (1998).
19. Lobkovsky, A., Gentges, S., Li, H., Morse, D. & Witten, T. A. Scaling properties of stretching ridges in a crumpled elastic sheet. *Science* **270,** 1482–1485 (1995).
20. Needleman, A. Computational mechanics at the mesoscale. *Acta Mater.* **48,** 105–124 (2000).
21. Chung, J.-S. & Ice, G. E. Automated indexing for texture and strain measurement with broad-bandpass x-ray microbeams. *J. Appl. Phys.* **86,** 5249–5255 (1999).
22. Tamura, N. *et al.* Strain and texture in Al-interconnect wires measured by x-ray microbeam diffraction. *Mater. Res. Soc. Proc.* **563,** 175–180 (1999).
23. Doherty, R. D. *et al.* Current issues in recrystallization: a review. *Mater. Sci. Eng. A* **238,** 219–274 (1997).
24. Humphreys, F. J. & Hatherly, M. *Recrystallization and Related Annealing Phenomena* (Pergamon, Oxford, 1995).
25. Kjelmstead, K. D. *Fundamentals of Structural Mechanics* (Prentice-Hall, London, 1997).
26. Landau, L. D. & Lifshitz, E. M. *Theory of Elasticity* (Pergamon, Oxford, 1986).
27. Hirsch, P. B. & Roberts, S. G. Comment on the brittle-to-ductile transition: a cooperative dislocation generation instability; dislocation dynamics and the strain-rate dependence of the transition temperature. *Acta Mater.* **44,** 2361–2371 (1995).
28. Khantha, M., Pope, D. P. & Vitek, V. Dislocation screening and the brittle-to-ductile transition: a Kosterlitz-Thouless type instability. *Phys. Rev. Lett.* **73,** 684–687 (1994).
29. Huang, Y., Xue, Z., Gao, H., Nix, W. D. & Xia, Z. C. A study of microindentation hardness tests by mechanism-based strain gradient plasticity. *J. Mater. Res.* **15,** 1786–1796 (2000).
30. Fleck, N. A. & Hutchinson, J. W. Strain-gradient plasticity. *Adv. Appl. Mech.* **33,** 295–361 (1997).

Acknowledgements

We thank H. Weiland, A. El-Azab, D. Maroudas and I. C. Noyan for discussions, and K.-S. Chung, W. Liu, J.-S. Chung, N. Tamura, E. Williams, W. P. Lowe and E. Dufresne for their contributions during this work. W.Y. is an ORISE fellow. The measurements were performed on the MHATT-CAT beam line at the Advanced Photon Source (APS), which is supported by the US Department of Energy, Office of Science. This research was sponsored by the US Department of Energy Basic Energy Sciences, Division of Materials Sciences, under contract with Oak Ridge National Laboratory, managed by UT-Battelle, LLC.

Competing interests statement

The authors declare that they have no competing financial interests.

Correspondence and requests for materials should be addressed to B.C.L. (e-mail: bcl@ornl.gov).

© 2002 Macmillan Magazines Ltd